Multifrequency inversion of global ambient seismic sources

Geophysical Journal International

Geophys. J. Int. (2021) **225,** 1616–1623
Advance Access publication 2021 February 6
GJI Seismology

doi: 10.1093/gji/ggab050

Multifrequency inversion of global ambient seismic sources

L.A. Ermert [1], K. Sager,[2] T. Nissen-Meyer[3] and A. Fichtner [4]

[1] *Department of Earth and Planetary Sciences, Harvard University, Cambridge, MA* 02138*, USA. E-mail: lermert@fas.harvard.edu*
[2] *Department of Earth, Environmental and Planetary Sciences, Brown University, Providence, RI* 02912*, USA*
[3] *Department of Earth Sciences, University of Oxford, Oxford OX*1 3*AN, UK*
[4] *Department of Earth Sciences, ETH Zurich* 8092*, Switzerland*

Accepted 2021 February 3. Received 2021 January 12; in original form 2020 August 31

SUMMARY

We develop and apply a method to constrain the space- and frequency-dependent location of ambient noise sources. This is based on ambient noise cross-correlation inversion using numerical wavefield simulations, which honour 3-D crustal and mantle structure, ocean loading and finite-frequency effects. In the frequency range from 3 to 20 mHz, our results constrain the global source distribution of the Earth's hum, averaged over the Southern Hemisphere winter season of 9 yr. During Southern Hemisphere winter, the dominant sources are largely confined to the Southern Hemisphere, the most prominent exception being the Izu-Bonin-Mariana arc, which is the most active source region between 12 and 20 mHz. Generally, strong hum sources seem to be associated with either coastlines or bathymetric highs. In contrast, deep ocean basins are devoid of hum sources. While being based on the relatively small number of STS-1 broad-band stations that have been recording continuously from 2004 to 2013, our results demonstrate the practical feasibility of a frequency-dependent noise source inversion that accounts for the complexities of 3-D wave propagation. It may thereby improve full-waveform ambient noise inversions and our understanding of the physics of noise generation.

Key words: Inverse theory; Seismic noise; Surface waves and free oscillations.

1 INTRODUCTION

In the absence of earthquakes, seismic stations record a wealth of ambient signals, the sources of which have been studied extensively in order to understand their physical origin, and to improve interferometric imaging of the Earth's interior (e.g. Aster *et al.* 2008; Stutzmann *et al.* 2009; Yao & van der Hilst 2009; Traer *et al.* 2012; Reading *et al.* 2014; Gal *et al.* 2015; Juretzek & Hadziioannou 2017). At periods above ∼1 s, interactions of ocean waves with the solid Earth are considered the strongest and most persistent sources. Models describing them are often presented in the form of geographically varying amplitude spectra or power-spectral densities (PSDs, e.g. Nishida & Fukao 2007; Ardhuin *et al.* 2011; Ermert *et al.* 2017). In addition to being required in ambient noise waveform inversion (Tromp *et al.* 2010; Basini *et al.* 2013; Fichtner *et al.* 2017; Sager *et al.* 2018a, 2020; Fichtner & Tsai 2019), such models provide a valuable link to oceanography via maps of ocean microseism pressure sources (Gualtieri *et al.* 2013; Ardhuin *et al.* 2015, 2019; Farra *et al.* 2016; Deen *et al.* 2018).

The characterization of ambient seismic sources is most commonly based on beamforming and matched field processing (e.g. Gerstoft & Tanimoto 2007; Gal *et al.* 2015, 2018; Juretzek & Hadziioannou 2017; Gal & Reading 2019), grid search (Shapiro *et al.* 2006), back-projection of cross-correlation amplitudes (Stehly *et al.* 2006; Brzak *et al.* 2009; Tian & Ritzwoller 2015; Retailleau *et al.* 2017) and cross-correlation inversion (Nishida & Fukao 2007; Harmon *et al.* 2010; Hanasoge 2013; Sadeghisorkhani *et al.* 2016; Ermert *et al.* 2017; Datta *et al.* 2019; Xu *et al.* 2019, 2020).

Previous inversions for ambient seismic source PSD either used a simplified model of wave propagation, mainly plane waves in homogeneous media (e.g. Harmon *et al.* 2010; Sadeghisorkhani *et al.* 2016) or, alternatively, fixed the frequency dependence of the amplitude spectrum (e.g. Nishida & Fukao 2007; Ermert *et al.* 2017). However, both numerical modelling (Stutzmann *et al.* 2012; Gualtieri *et al.* 2013, 2014; Farra *et al.* 2016) and observations (e.g. Peterson 1993; Stehly *et al.* 2006; Traer *et al.* 2012; Juretzek & Hadziioannou 2017) indicate that the spectra of ambient noise sources are highly variable in space and frequency, most likely because wavefield excitation depends on bathymetry and local ocean wave conditions. At the same time, recent studies have underlined the importance of accounting for nearby sources and for lateral velocity variations in the localization of noise sources (Juretzek & Hadziioannou 2017; Ward Neale *et al.* 2017; Gal *et al.* 2018; Takagi *et al.* 2018), thereby questioning the plane-wave approximation.

In this context, we develop and apply an inversion technique that constrains the space- and frequency-dependent distribution of ambient noise source PSD, while accounting for 3-D crust and mantle structure, ocean loading, and finite-frequency sensitivity. Building on the fixed-spectrum inversion technique of Ermert *et al.* (2017), our main goals are (1) to demonstrate the feasibility of

jointly inverting for the space- and frequency-dependence of noise sources and (2) to investigate the global-scale source distribution of ambient noise at long periods from 50 to 350 s, commonly referred to as the Earth's hum (e.g. Nishida & Kobayashi 1999).

2 MULTIFREQUENCY SOURCE INVERSION

Our inversion rests on gradient-based iterative optimization, aiming to match the causal/anticausal asymmetry of observed and synthetic noise correlations to within their estimated errors. This requires the formulation of a forward problem, the definition of a misfit functional, the computation of sensitivity kernels and a suitable parametrization of the source PSD. These components will be covered in the following paragraphs.

2.1 Forward modelling, measurements and sensitivity kernels

The i, j-component of the frequency-domain correlation tensor $\mathbf{C}$ can be expressed in the form of a representation theorem (e.g. Tromp *et al.* 2010; Fichtner 2014; Ermert *et al.* 2017)

$$C_{ij,ab}(\omega) = \int G_{jm}(\boldsymbol{x}_b, \boldsymbol{\xi}, \omega)\, G^*_{in}(\boldsymbol{x}_a, \boldsymbol{\xi}, \omega)\, S_{nm}(\boldsymbol{\xi}, \omega)\, \mathrm{d}\boldsymbol{\xi}\,, \tag{1}$$

where $\boldsymbol{x}_a$ and $\boldsymbol{x}_b$ are two station locations, ω is the circular frequency, and G_{jm} is the j-component of the Green's function due to a unit force in m-direction. The symbol $S_{nm}(\boldsymbol{\xi}, \omega)$ denotes the source PSD, that is, the correlation tensor of sources acting at position $\boldsymbol{\xi}$ in n- and m-directions, respectively. Integration is over the Earth's surface, and summation over repeated indices is implied.

To quantify the discrepancy between synthetic correlations $C_{ij,ab}$ and observed correlations $C^{\mathrm{obs}}_{ij,ab}$, we measure their respective asymmetry in the form of the logarithmic ratio of signal energy on the causal and anticausal branches,

$$A_{ij,ab} = \ln \frac{\int \left[w_{ij,ab}(t) C_{ij,ab}(t)\right]^2 \mathrm{d}t}{\int \left[w_{ij,ab}(-t) C_{ij,ab}(t)\right]^2 \mathrm{d}t}\,, \tag{2}$$

with the observed asymmetry $A^{\mathrm{obs}}_{ij,ab}$ defined accordingly. The function $w_{ij,ab}$ is a time window used to isolate fundamental-mode surface waves. For the calculation of $C^{\mathrm{obs}}_{i,j}$, we refer to Section 3.1 and the supplementary material. The asymmetry measurement avoids the use of absolute amplitudes, and is robust with respect to inaccuracies of the 3-D earth model (Sager *et al.* 2018b). Based on (2), we obtain the least-squares asymmetry misfit

$$\chi = \frac{1}{2} \sum_{i,j} \sum_{a,b} \left(A_{ij,ab} - A^{\mathrm{obs}}_{ij,ab}\right)^2\,, \tag{3}$$

by summing over station pairs (a, b) and components (i, j) that we wish to include.

Since the size of the model parameter space, detailed in the following section, excludes the application of Monte Carlo methods, we apply gradient-based optimization to find plausible ambient source models. Sensitivity kernels quantify the misfit change in response to an infinitesimal perturbation of the space- and frequency-dependent noise sources, $\delta \tilde{S}_{nm}(\boldsymbol{\xi}, \omega)$ (e.g. Tarantola 2005; Fichtner 2010). A sensitivity kernel can be expressed as (e.g. Tromp *et al.* 2010; Fichtner 2014)

$$K_{nm}(\boldsymbol{\xi}, \omega) = \sum_{i,j} \sum_{a,b} g_{ij,ab}(\omega)\, G_{jm}(\boldsymbol{x}_b, \boldsymbol{\xi}, \omega)\, G^*_{in}(\boldsymbol{x}_a, \boldsymbol{\xi}, \omega)\,, \tag{4}$$

where $g_{ij,ab}(\omega)$ is the adjoint source. An explicit expression of $g_{ij,ab}(\omega)$ for a fixed frequency and the asymmetry misfit (3) can be found in Ermert *et al.* (2017).

To evaluate the forward modelling eq. (1) and the sensitivity kernel expression (4), we require the Green's tensor $\mathbf{G}(\boldsymbol{x}, \boldsymbol{\xi}, \omega)$ between receiver locations at the surface $\mathbf{x}$ and gridpoints $\boldsymbol{\xi}$ of the discretized source distribution. To account for 3-D Earth structure, ocean loading, ellipticity and rotation, we approximate the Green's tensor numerically, using the spectral-element wave propagation solver SPECFEM3D_globe (Komatitsch & Tromp 2002a,b). This allows us to pre-compute a Green's function database, which then serves to rapidly evaluate eqs (1) and (4) in the course of the iterative misfit minimization.

2.2 Frequency parametrization of the source spectrum

Since the PSD at a large number of discrete frequencies is unlikely to be resolvable, we represent the frequency-dependence of $S_{nm}(\boldsymbol{\xi}, \omega)$ in terms of a small number N of orthogonal basis functions $s^k(\omega)$, with $k = 1, ..., N$, that is,

$$S_{nm}(\boldsymbol{\xi}, \omega) = \sum_{k=1}^{N} s^k(\omega) S^k_{nm}(\boldsymbol{\xi})\,, \tag{5}$$

where $S^k_{nm}(\boldsymbol{\xi})$ contains the purely space-dependent contribution. Multiplying the space-frequency-dependent kernel (4) by $s^k(\omega)$ and integrating over ω, yields space-dependent kernels for the individual space-dependent sources $S^k_{nm}(\boldsymbol{\xi})$. In the following real-data and synthetic inversions we chose the basis functions $s^k(\omega)$ to be orthogonal sinc functions.

Fig. 1 illustrates vertical-component measurements with corresponding vertical–vertical-component sensitivity kernels K_{zz} for station pair CN.YKW1–CN.FRB in the frequency bands 3–6, 6–12 and 12–20 mHz. For each band, we take a separate measurement in the expected Rayleigh-wave windows. The window centre and half-width are adapted to the respective frequency range in order to account for surface wave dispersion. The lower panels display normalized sensitivity kernels, averaged over the basis function index k. Both frequency content and window width affect the sensitivity distribution, which, furthermore, depends on the initial noise source PSD used to model correlations. For this example, we used a spatially uniform PSD with frequency dependence given by a Hann window between 1 and 30 mHz, peaking at 15 mHz.

3 APPLICATION–FREQUENCY-DEPENDENT SOURCES OF THE EARTH'S HUM

In the following paragraphs, we describe the application of our method to the Earth's hum, previously studied by several authors (e.g. Nishida & Kobayashi 1999; Ekström 2001; Rhie & Romanowicz 2004, 2006; Nishida & Fukao 2007; Traer *et al.* 2012; Nishida 2014; Traer & Gerstoft 2014; Ardhuin *et al.* 2015; Maurya *et al.* 2019).

3.1 Data

We analyse data recorded on the LHZ channels of publicly available STS-1 stations, the distribution of which is shown in Fig. 2. The higher station density in the Northern Hemisphere leads to a higher resolution of noise sources in the Southern Hemisphere, because

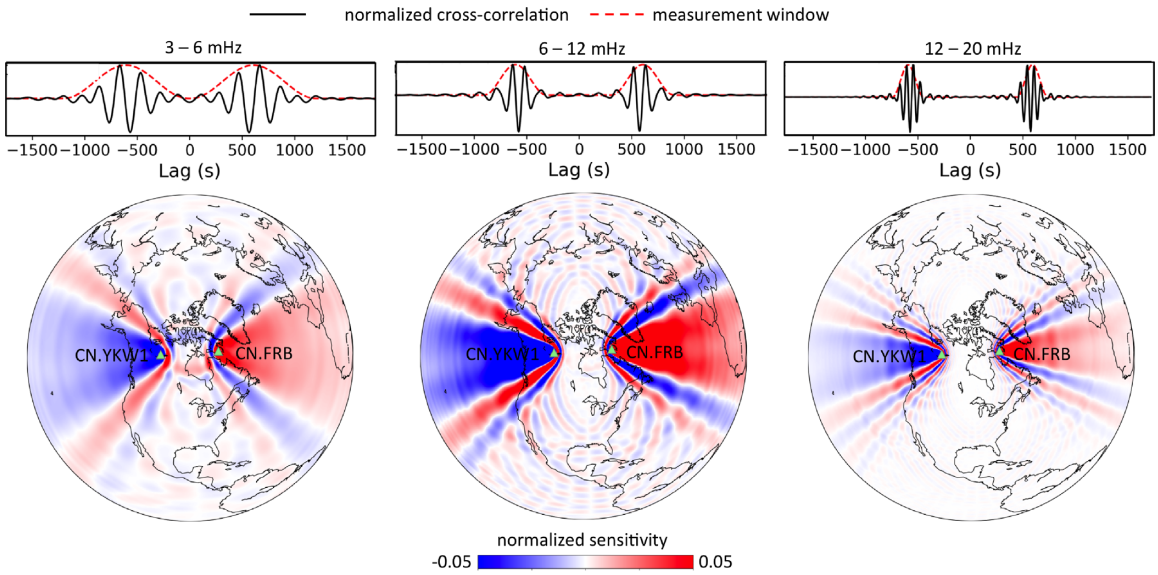

Figure 1. Illustration of sensitivity kernels used for the frequency-dependent inversion. Top panels show vertical–vertical component synthetic cross-correlations filtered in three different frequency, 3–6 mHz (left-hand panel), 6–12 mHz (centre panel) and 12–20 mHz (right-hand panel). Measurement windows $w(\pm t)$ centred on the causal and anticausal Rayleigh wave arrivals are indicated by red dashed curves. The maps below show the normalized sensitivity to the vertical–vertical component of the ambient source PSD (colour scale is clipped for better visibility) of each measurement on the differently filtered and windowed cross-correlations. The underlying earth model is S40RTS.

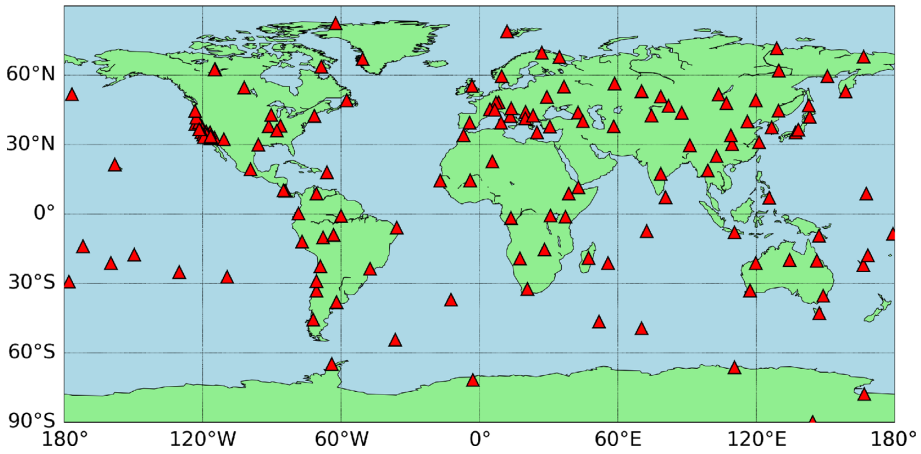

Figure 2. Distribution of seismic stations with vertical-component STS-1 sensors used in this study. All stations have been operating continuously between 2004 and 2013.

sensitivity kernels are hyperbolic jets that refocus near the antipoles (e.g. Ermert *et al.* 2017; Fichtner & Tsai 2019). We therefore focus on the analysis of data for the Southern Hemisphere winter months (June–August), when dominant hum sources are expected in the Southern Hemisphere. Data from the 3 months are averaged over 9 yr, from 2004 to 2013, excluding 2005 (the year following the Sumatra–Andaman earthquake), to increase the signal-to-noise ratio.

Details of the data processing, including the muting of earthquakes (Ekström 2001) are described in Supplement 1. In general, we avoid nonlinear processing, which may introduce artefacts by breaking the linear wave propagation physics (Fichtner *et al.* 2020). Prior to making asymmetry measurements, we filter noise correlations in three frequency bands, 3–6, 6–12 and 12–20 mHz, each of which contributes to the total misfit.

Following the approach described in Ermert *et al.* (2017), we estimate the standard deviation of the asymmetry measurements by comparing noise correlations between the nearly colocated stations of the Yellowknife array and stations elsewhere. This provides appropriate weights for the frequency-dependent contributions to the misfit functional, and also indicates when iterations should be stopped to avoid overfitting.

3.2 Spectral and spatial starting models and Green's function database

To obtain a spectral starting model, we analyze PSDs of ground velocity observed at Geoscope STS-1 stations, which have mostly low noise levels at long periods and are globally distributed (Stutzmann *et al.* 2000). The 3-month median PSDs are shown in Fig. 3(a). Despite containing the spectrum of both Earth's seismic response and the hum sources, we use the 9-yr median, shown as yellow line in Fig. 3(a), as a plausible spectral starting model. Xu *et al.* (2020)

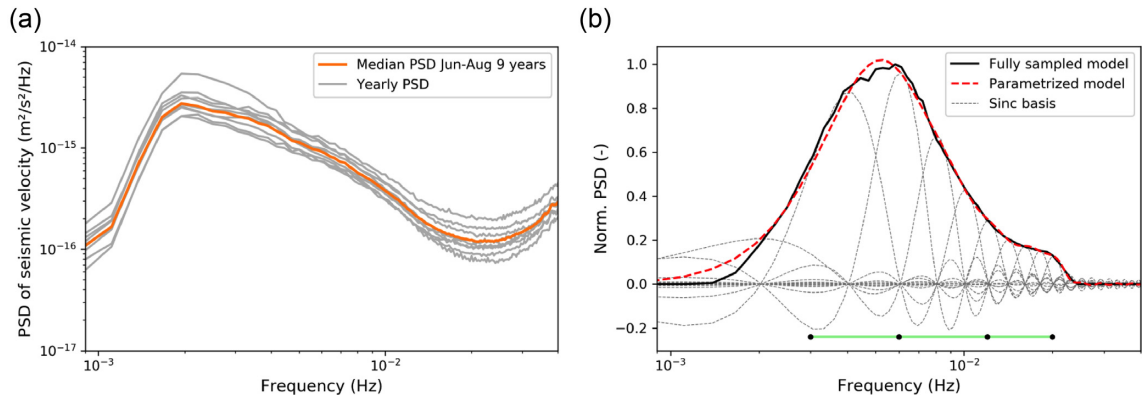

Figure 3. Spectral starting model and spectral parametrization. (a) Observed yearly median of seismic velocity PSD at all Geoscope stations. The orange curve shows the median of the nine years (2004–2013, excluding 2005) and is used as spectral starting model for the source PSD. (b) Starting source PSD (black line), which corresponds to the normalized tapered observed velocity PSD from the left, and parametrized source PSD (red dashed line). Grey dashed lines show the sinc tapers used as basis functions in the frequency domain. The green line illustrates the three frequency ranges investigated, separated by black dots.

also build a starting model from observed autocorrelations (equivalent to PSDs), albeit deconvolving assumed homogeneous Green's functions.

A Tukey taper isolated the frequency range of interest and down-weighs the lowest-frequency contributions of the starting model at 2–3 mHz, which is expected to suffer from elevated instrumental and barometric noise. Since the measurement of noise correlation asymmetry cannot constrain absolute amplitudes of noise sources, we normalize the spectral starting model to a maximum value of 1. For the spectral parametrization of the PSD we use 12 orthogonal zero-phase sinc tapers, illustrated in Fig. 3(b).

The vertical–vertical component of the spatial starting model is homogeneous for each basis function, covering oceans and continents. Since our analysis is limited to vertical–vertical-component correlations, all other components of the source PSD distribution are kept at zero throughout the inversion, neglecting the excitation of vertical-component signals by horizontal sources (see Section 4).

For the computation of the Green's function database needed for both synthetic correlations and sensitivity kernels, we employ the spectral-element solver SPECFEM3D_globe (Komatitsch & Tromp 2002a,b). The earth model is S40RTS (Ritsema *et al.* 2011), combined with crustal model Crust2.0 (Bassin *et al.* 2000), topography and ocean loading.

3.3 Iterative optimization

The inverse problem for this particular application can be formulated as follows. We drop the subscripts for correlation components on the spatial coefficients $S^k(\boldsymbol{\xi})$ describing the source model, as we focus on the vertical–vertical:

$$S^{k,\text{optimal}}(\boldsymbol{\xi}) = \underset{S^k(\boldsymbol{\xi})}{\arg\min} \left(\sum_{i,j} w_j \frac{1}{2} \left[A_j^{obs} - A_j \right]^2 \right), \tag{6}$$

where A is defined in eq. (2), index i refers to station pair and index j refers to the filter band. The weighting w_j for each frequency band is set to the inverse estimated data variance (see Section 3.1). Filtering is necessary because A does not carry frequency-dependent information, so that only using different filter bands allows us to distinguish sources predominantly occurring in different frequency bands. The spatial coefficients S^k are represented in our model as values on a discrete grid at the Earth's surface.

The asymmetry measurement A depends on the cross-correlations and consequently on S in a non-linear fashion. Therefore, we choose an iterative inversion strategy, and minimize the initial misfit using a simple steepest-descent algorithm. Though more powerful nonlinear optimization techniques exist (e.g. Nocedal & Wright 2006), steepest descent allows us to interpret each of the successive updates more easily, as the algorithm always follows the current negative gradient without taking previous steps into account. To avoid artefacts, we apply a Gaussian smoothing filter with an initial standard deviation of 600 km, successively decreased to 300 km for the six higher-frequency tapers.

After a total of nine iterations, the overall misfit has plateaued. The average misfit reduction is ∼25 per cent. In the higher frequency bands, it is ∼30 and ∼40 per cent, respectively. The lowest frequency band converges more slowly, since the sensitivity of cross-correlation asymmetry to noise sources at long periods is decreased as an effect of lower attenuation (a related point was discussed in Nishida & Fukao 2007). A more detailed misfit analysis can be found in Supplement S2. The final hum source PSD model is displayed in Fig. 4.

4 DISCUSSION

4.1 Resolution

We estimate spatial and spectral resolution of the model using a series of synthetic inversions, shown in Supplement S3, as an easily interpretable proxy. The results of the recovery tests dictate the allowable level of detail in the interpretation.

Fig. S3.1 (global recovery test) confirms that the antipodal focusing of sensitivity from predominantly Northern Hemisphere stations causes resolution to be better in the Southern Hemisphere. Hence, while horizontal smearing in the South Pacific is on the order of 1500 km, it is closer to 3000 km in the North Atlantic. Considering a central wavelength of around 500 km, this indicates, as expected, that resolution is limited by coverage and not by bandwidth.

From Fig. S3.2 (scaled Cartesian recovery test) we infer that each measurement indeed prefers updates of the spectral basis functions within its corresponding frequency band. This allows us to constrain the locations of the dominant ambient sources with limited inter-frequency smearing.

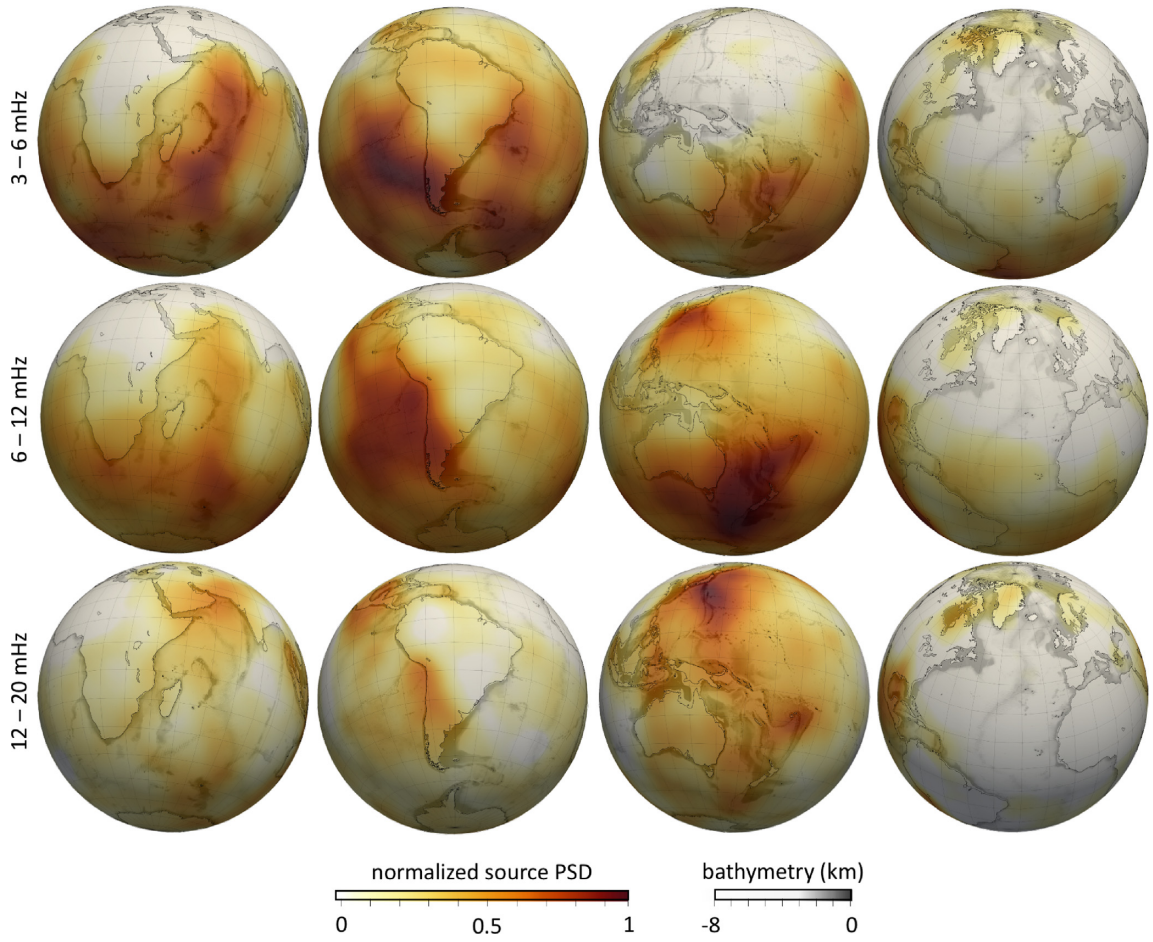

Figure 4. Selected views of the final hum source PSD model. Shown are normalized PSDs after filtering the frequency-dependent model in the respective frequency bands. This is achieved by expanding the frequency-dependent model using its sinc basis, then windowing it in the Fourier domain using a Tukey taper that covers the frequency range of interest, and finally summing over the relevant frequency band. Greyscale in the background shows bathymetry.

4.2 Dominant features

Comparing the three frequency bands, we note that the dominant hum source regions for Southern Hemisphere winter in the 3–6 and 6–12 mHz bands are mostly located in the Southern Hemisphere oceans. In particular, the west coast of Chile, the western Indian Ocean near the Central Indian Ridge and the Southwest Pacific appear prominently.

In the 12–20 mHz band, there are several similarities to the 6–12 mHz band, including strong sources off the Chilean coast and near Fiji. However, distinct differences also exist. For instance, the strongest source region between 12 and 20 mHz appears in the Izu-Bonin region, that is, in the Northern Hemisphere. As expected, continental areas mostly show comparatively weak hum source PSD, though the inversion does not decrease the initially homogeneous source PSD to exactly zero on the continents.

All of these dominant sources are located in the proximity of either coastlines or bathymetric highs, including, for instance, the Chile Ridge, the Lord Howe Rise, the Kermadec Ridge, the Rio Grande Rise, the Ninety East Ridge and the Izu-Bonin-Mariana Arc. In contrast, deep oceanic basins, such as the Argentine, Brazil and Angola Basins, or the North- and Southwest Pacific Basins, generally do not host notable hum sources.

Another dominant feature, though in a different sense, is the North Atlantic, which is practically devoid of hum sources during Southern Hemisphere winter.

A further remarkable aspect of the hum source model is the strong frequency dependence. While, for instance, the Izu-Bonin region is the dominant source in the 12–20 mHz range, it does not feature any notable activity between 3 and 6 mHz.

4.3 Comparison to previous hum source models

To discuss specific aspects of our model, we draw on previous results from modelling as well as observations (e.g. Nishida & Fukao 2007; Traer *et al.* 2012; Deen *et al.* 2018). As they cover different observation periods, some differences in the inferred source patterns may be due to yearly variations of ocean infragravity wave and hum excitation. Deen *et al.* (2018) used the mechanism proposed by Ardhuin *et al.* (2015) to model the PSDs of hum at stations surrounding the Indian Ocean. They considered hum source pressure PSDs for July–September 2013 in the 7–20 mHz range. Traer *et al.* (2012) based their analysis on seismic time-series, using beamforming and correlation of seismic PSD with ocean wave height. Their study focused the Southern Hemisphere winter of 2011 and the frequency band of 5–20 mHz. The work of Deen *et al.* (2018) and Traer *et al.* (2012) roughly covers our middle and upper frequency bands. Finally, Nishida & Fukao (2007) performed an inversion with a smooth spectral parametrization, spherically symmetric earth model and a

fixed spectrum of the hum sources. Their data span the years 1988–2000 and a frequency range of 2–10 mHz, approximately coinciding with our lower and middle frequency bands.

All of these models agree on the presence of strong sources in the eastern Pacific, off the Chilean coast. Our model suggests this source to be most active in the 3–12 mHz range, shifting slightly southwards for lower frequencies. Traer *et al.* (2012) observe the highest correlation of seismic and wave height time series near the coast. Our model suggests that sources may also act at larger distance from the coast. Though smearing caused by limited spatial resolution certainly broadens the perceived source regions, the synthetic recovery test shown in Supplement S3 indicates that the eastern Pacific source is significantly broader than the approximate resolution length. This supports the inference of strong hum sources located several thousand kilometers east of the South American coast. These sources may not necessarily spread evenly across this region. Instead, a number of more localized sources may act together in creating an overall strong hum source.

In addition to the Chilean coast, the middle frequency band shows a prominent source between Australia and New Zealand. In the highest frequency band, the dominant location shifts to the Izu-Bonin trench region. The 6–20 mHz range of our model shows good agreement with the model of Traer *et al.* (2012), who found Chilean coast and adjacent regions, as well as the New Zealand–Australian region as strongest hum sources in Southern Hemisphere winter. The South African coast, which does not appear prominently in our model, also shows weaker beampower and weaker correlation of oceanic and seismic time series in their study. Of all the source regions imaged in the Northern Hemisphere by Traer *et al.* (2012), the Izu-Bonin region is the only one with both comparatively high beampower and high correlation between seismic and ocean wave time series. It therefore seems plausible that our inversion retrieves only this source region in the North Hemisphere. One may hypothesize that the strong hum sources in North Hemisphere summer in this region are linked to the occurrence of typhoons: Nishida (2017) shows a temporal coincidence between ocean ambient seismic sources at 12.5 mHz along the East Asian ocean–continent boundaries. Inversions with higher temporal resolution could clarify if the two phenomena are indeed coincident. Very careful processing would be required to obtain a sufficient signal from short observation windows.

When compared to the modelled source distribution of Deen *et al.* (2018), the detailed patterns are less similar. Although the Chilean coast, New Zealand and Izu-Bonin also feature coastal hum sources in their model, other important regions such as the South African coast are not prominent in our model. However, we remark that the North Atlantic is consistently quiet, with source spectral density dropping by approximately 15–20 db compared to the dominant sources in their model.

4.4 Apparent continental sources

While most authors agree that ocean infragravity waves interacting with the sea floor or sloping shelf cause the long-period Rayleigh waves of the hum (e.g. Rhie & Romanowicz 2006; Traer & Gerstoft 2014; Ardhuin *et al.* 2015), also coupling between the atmosphere and the solid Earth has been proposed as a possible source mechanism (Nishida 2014). Most continental sources in our model are weak and most likely smeared from strong sources in the ocean. This suggests that any continental hum sources are comparatively weak.

To exclude continental hum sources *a priori*, we also tested inversions where non-zero PSD was allowed only in the oceans. The resulting models is dominated by artifacts (see Supplement S4), suggesting instability of the inversion scheme in the presence of large, source-free regions. Hence, including such prior constraints remains a subject of future methodological developments.

4.5 Further steps

The retrieval of frequency-dependent noise source distributions, which show consistency with previous studies, is an important step towards both an improved understanding of ambient seismic source physics. It also contributes to improved full-waveform ambient noise inversions (Sager *et al.* 2020), when dense arrays permitting direct inversion (as in de Ridder & Maddison 2018; Lehujeur & Chevrot 2020) are unavailable. Yet, the current noise source inversion method is still limited by the measurement strategy. While rather insensitive to 3-D Earth structure (Sager *et al.* 2018a), the asymmetry of causal and anticausal Rayleigh waves is from the outset unable to constrain the absolute PSD. Furthermore, other potentially useful information, contained in different coherent parts of the noise correlations, is ignored. Finally, compared to waveforms or amplitudes at a fixed lag time, the measurement depends nonlinearly on the cross-correlation, which has some effects that are discussed further in the supplementary material. For the presented global case, the recovery test and the consistency with earlier studies lead us to conclude that this does not present a major obstacle.

Improved measurements should ideally strike a reasonable balance between simplicity, exploitation of more information and relative insensitivity to Earth structure. Furthermore, the effect of processing should be reduced or accounted for, possibly as suggested by Fichtner *et al.* (2020). Extracting additional information, for instance from major-arc surface waves (Nishida *et al.* 2009) or radial components (Xu *et al.* 2018, 2019) is likely to further improve resolution for vertical sources.

The influence of (effective) horizontal-component ambient noise sources is a relatively recent field of study (Nishida 2014; Juretzek & Hadziioannou 2017) and was out of scope for the current application. However, as it is assumed that Love surface waves are excited by effective horizontal forces (Saito 2010; Ardhuin 2018) resulting from the interactions of vertical pressure with undulating ocean bathymetry, Rayleigh surface waves must be excited by those sources, too. The method we present functions no differently for horizontal-component sources, and including them is therefore an important future step of this work.

DATA AND RESOURCES

Observational data used in this study were obtained from the IRIS Data Management Center. IRIS Data Services are funded through the Seismological Facilities for the Advancement of Geoscience and EarthScope (SAGE) Proposal of the National Science Foundation under Cooperative Agreement EAR-1261681. Data processing was conducted using Obspy Krischer *et al.* (2015). Processing and cross-correlation scripts can be accessed online at: https://github.com/lermert/ants_2.

Specfem3D_Globe is provided by the computational infrastructure for geodynamics at:

https://geodynamics.org/cig/software/specfem3d_globe/

Finally, the modelling software for cross-correlations can be accessed at:

https://github.com/lermert/noisi.

ACKNOWLEDGEMENTS

We gratefully acknowledge the insightful and detailed reviews of Sjoerd de Ridder and an anonymous reviewer. We also wish to thank Simon Stähler, Eléonore Stutzmann and Fabrice Ardhuin for comments and discussions that have led to improvements of this work, as well as Dylan Mikesell, Jeroen Ritsema and an anonymous reviewer for their insightful comments on an earlier version of the manuscript. LE wishes to thank Naiara Korta Martiartu for help with inverse theory. This research was supported by the Swiss National Science Foundation under grants P2EZP2_175124 and P2EZP2_184379, and by US NSF and UK NERC under joint grant NE/R012199/1. Computations were run at the Swiss National Supercomputing Centre under project s741 (Green's function simulations) and on the UK National Supercomputer ARCHER under TNM's NERC remit (data processing and iterative inversion).

REFERENCES

Ardhuin, F., 2018. Large-scale forces under surface gravity waves at a wavy bottom: a mechanism for the generation of primary microseisms, *Geophys. Res. Lett.,* **45**(16), 8173–8181.

Ardhuin, F., Stutzmann, E., Schimmel, M. & Mangeney, A., 2011. Ocean wave sources of seismic noise, *J. geophys. Res.,* **116,** doi:10.1029/2011JC006952.

Ardhuin, F., Gualtieri, L. & Stutzmann, E., 2015. How ocean waves rock the earth: two mechanisms explain microseisms with periods 3 to 300 s, *Geophys. Res. Lett.,* **42**(3), 765–772.

Ardhuin, F., Gualtieri, L. & Stutzmann, E., 2019. *Physics of Ambient Noise Generation by Ocean Waves,* Cambridge Univ. Press.

Aster, R.C., McNamara, D.E. & Bromirski, P.D., 2008. Multidecadal climate-induced variability in microseisms, *Seismol. Res. Lett.,* **79**(2), 194–202.

Basini, P., Nissen-Meyer, T., Boschi, L., Casarotti, E., Verbeke, J., Schenk, O. & Giardini, D., 2013. The influence of nonuniform ambient noise on crustal tomography in Europe, *Geochem. Geophys. Geosyst.,* **14**(5), 1471–1492.

Bassin, C., Laske, G. & Masters, G., 2000. The current limits of resolution for surface wave tomography in North America, *EOS, Trans. Am. geophys. Un.,* **81,** F897.

Brzak, K., Gu, Y.J., Ökeler, A., Steckler, M. & Lerner-Lam, A., 2009. Migration imaging and forward modeling of microseismic noise sources near southern Italy, *Geochem. Geophys. Geosyst.,* **10**(1), Q01012, doi:10.1029/2008GC002234.

Datta, A., Hanasoge, S. & Goudswaard, J., 2019. Finite-frequency inversion of cross-correlation amplitudes for ambient noise source directivity estimation, *J. geophys. Res.,* **124**(7), 6653–6665.

de Ridder, S.A.L. & Maddison, J.R., 2018. Full wavefield inversion of ambient seismic noise, *Geophys. J. Int.,* **215**(2), 1215–1230.

Deen, M., Stutzmann, E. & Ardhuin, F., 2018. The Earth's hum variations from a global model and seismic recordings around the Indian Ocean, *Geochem. Geophys. Geosyst.,* **19**(10), 4006–4020.

Ekström, G., 2001. Time domain analysis of earth's long-period background seismic radiation, *J. geophys. Res.,* **106**(B11), 26 483–26 493.

Ermert, L., Sager, K., Afanasiev, M., Boehm, C. & Fichtner, A., 2017. Ambient seismic source inversion in a heterogeneous Earth—theory and application to the Earth's hum, *J. geophys. Res.,* **122**(11), 9184–9207.

Farra, V., Stutzmann, E., Gualtieri, L., Schimmel, M. & Ardhuin, F., 2016. Ray-theoretical modeling of secondary microseism P waves, *Geophys. J. Int.,* **206**(3), 1730.

Fichtner, A., 2010. *Full Seismic Waveform Modelling and Inversion.,* Springer.

Fichtner, A., 2014. Source and processing effects on noise correlations, *Geophys. J. Int.,* **197,** 1527–1531.

Fichtner, A. & Tsai, V., 2019. *Theoretical Foundations of Noise Interferometry,* Cambridge Univ. Press.

Fichtner, A., Stehly, L., Ermert, L. & Boehm, C., 2017. Generalized interferometry – I: theory for interstation correlations, *Geophys. J. Int.,* **208**(2), 603.

Fichtner, A., Bowden, D. & Ermert, L., 2020. Optimal processing for seismic noise correlations, *Geophys. J. Int.,* **223**(3), 1548–1564.

Gal, M. & Reading, A., 2019. *Beamforming and Polarization Analysis,* Cambridge Univ. Press.

Gal, M., Reading, A.M., Ellingsen, S.P., Gualtieri, L., Koper, K.D., Burlacu, R., Tkalčić, H. & Hemer, M.A., 2015. The frequency dependence and locations of short-period microseisms generated in the southern ocean and west pacific, *J. geophys. Res.,* **120**(8), 5764–5781.

Gal, M., Reading, A., Rawlinson, N. & Schulte-Pelkum, V., 2018. Matched field processing of three-component seismic array data applied to Rayleigh and Love microseisms, *J. geophys. Res.,* **123**(8), 6871–6889.

Gerstoft, P. & Tanimoto, T., 2007. A year of microseisms in southern California, *Geophys. Res. Lett.,* **34**(20), L20304, doi:10.1029/2007GL031091.

Gualtieri, L., Stutzmann, E., Capdeville, Y., Ardhuin, F., Schimmel, M., Mangeney, A. & Morelli, A., 2013. Modelling secondary microseismic noise by normal mode summation, *Geophys. J. Int.,* **193**(3), 1732–1745.

Gualtieri, L., Stutzmann, E., Farra, V., Capdeville, Y., Schimmel, M., Ardhuin, F. & Morelli, A., 2014. Modelling the ocean site effect on seismic noise body waves, *Geophys. J. Int.,* **197**(2), 1096.

Hanasoge, S.M., 2013. Measurements and kernels for source-structure inversions in noise tomography, *Geophys. J. Int.,* **196**(2), 971–985.

Harmon, N., Rychert, C. & Gerstoft, P., 2010. Distribution of noise sources for seismic interferometry, *Geophys. J. Int.,* **183**(3), 1470.

Juretzek, C. & Hadziioannou, C., 2017. Linking source region and ocean wave parameters with the observed primary microseismic noise, *Geophys. J. Int.,* **211**(3), 1640–1654.

Komatitsch, D. & Tromp, J., 2002a. Spectral-element simulations of global seismic wave propagation, part II: 3-D models, oceans, rotation, and gravity, *Geophys. J. Int.,* **150,** 303–318.

Komatitsch, D. & Tromp, J., 2002b. Spectral-element simulations of global seismic wave propagation, part I: validation, *Geophys. J. Int.,* **149,** 390–412.

Krischer, L., Megies, T., Barsch, R., Beyreuther, M., Lecocq, T., Caudron, C. & Wassermann, J., 2015. ObsPy: a bridge for seismology into the scientific Python ecosystem, *Comput. Sci. Discov.,* **8**(1), 014003.

Lehujeur, M. & Chevrot, S., 2020. Eikonal tomography using coherent surface waves extracted from ambient noise by iterative matched filtering—application to the large-N Maupasacq Array, *J. geophys. Res.,* **125**(6), doi:10.1029/2020JB019363.

Maurya, S., Taira, T. & Romanowicz, B., 2019. Location of seismic "hum" sources following storms in the north pacific ocean, *Geochem. Geophys. Geosyst.,* **20**(3), 1454–1467.

Nishida, K., 2014. Source spectra of seismic hum, *Geophys. J. Int.,* **199**(1), 416–429.

Nishida, K., 2017. Ambient seismic wave field, *Proc. Jpn. Acad., B,* **93**(7), 423–448.

Nishida, K. & Fukao, Y., 2007. Source distribution of Earth's background free oscillations, *J. geophys. Res.,* **112**(B6), B06306, doi:10.1029/2006JB004720.

Nishida, K. & Kobayashi, N., 1999. Statistical features of Earth's continuous free oscillations, *J. geophys. Res.,* **104**(B12), 28 741–28 750.

Nishida, K., Montagner, J.-P. & Kawakatsu, H., 2009. Global surface wave tomography using seismic hum, *Science,* **326**(5949), 112–112.

Nocedal, J. & Wright, S., 2006. *Numerical Optimization,* Springer Science & Business Media.

Peterson, J., 1993. Observations and modeling of seismic background noise, USGS Open File Report 93-322, pp. 94, https://doi.org/10.3133/ofr93322.

Reading, A.M., Koper, K.D., Gal, M., Graham, L.S., Tkalčić, H. & Hemer, M.A., 2014. Dominant seismic noise sources in the southern ocean and West Pacific, 2000–2012, recorded at the Warramunga seismic array, Australia, *Geophys. Res. Lett.,* **41**(10), 3455–3463.

Retailleau, L., Boué, P., Stehly, L. & Campillo, M., 2017. Locating microseism sources using spurious arrivals in intercontinental noise correlations, *J. geophys. Res.,* **122**(10), 8107–8120.

Rhie, J. & Romanowicz, B., 2004. Excitation of Earth's continuous free oscillations by atmosphere-ocean-seafloor coupling., *Nature,* **431**(7008), 552–556.

Rhie, J. & Romanowicz, B., 2006. A study of the relation between ocean storms and the Earth's hum, *Geochem. Geophys. Geosyst.,* **7**(10), doi:10.1029/2006GC001274.

Ritsema, J., Deuss, A., van Heijst, H.J. & Woodhouse, J.H., 2011. S40RTS: a degree-40 shear-velocity model for the mantle from new Rayleigh wave dispersion, teleseismic traveltime and normal-mode splitting function measurements, *Geophys. J. Int.,* **184,** 1223–1236.

Sadeghisorkhani, H., Gudmundsson, O., Roberts, R. & Tryggvason, A., 2016. Mapping the source distribution of microseisms using noise covariogram envelopes, *Geophys. J. Int.,* **205**(3), 1473.

Sager, K., Boehm, C., Ermert, L., Krischer, L. & Fichtner, A., 2018a. Sensitivity of seismic noise correlation functions to global noise sources, *J. geophys. Res.,* **123**(8), 6911–6921.

Sager, K., Ermert, L., Boehm, C. & Fichtner, A., 2018b. Towards full waveform ambient noise inversion, *Geophys. J. Int.,* **212**(1), 566–590.

Sager, K., Boehm, C., Ermert, L., Krischer, L. & Fichtner, A., 2020. Global-scale full-waveform ambient noise inversion, *J. geophys. Res.,* **125**(4),.

Saito, T., 2010. Love-wave excitation due to the interaction between a propagating ocean wave and the sea-bottom topography, *Geophys. J. Int.,* **182**(3), 1515.

Shapiro, N.M., Ritzwoller, M. & Bensen, G., 2006. Source location of the 26 sec microseism from cross-correlations of ambient seismic noise, *Geophys. Res. Lett.,* **33**(18), doi:10.1029/2006GL027010.

Stehly, L., Campillo, M. & Shapiro, N.M., 2006. A study of the seismic noise from its long-range correlation properties, *J. geophys. Res.,* **111**(B10), doi:10.1029/2005JB004237.

Stutzmann, E., Roult, G. & Astiz, L., 2000. Geoscope station noise levels, *Bull. seism. Soc. Am.,* **90**(3), 690–701.

Stutzmann, E., Schimmel, M., Patau, G. & Maggi, A., 2009. Global climate imprint on seismic noise, *Geochem. Geophys. Geosyst.,* **10**(11), Q11004.

Stutzmann, E., Ardhuin, F., Schimmel, M., Mangeney, A. & Patau, G., 2012. Modelling long-term seismic noise in various environments, *Geophys. J. Int.,* **191**(2), 707–722.

Takagi, R., Nishida, K., Maeda, T. & Obara, K., 2018. Ambient seismic noise wavefield in Japan characterized by polarization analysis of Hi-net records, *Geophys. J. Int.,* **215**(3), 1682–1699.

Tarantola, A., 2005. *Inverse Problem Theory and Methods for Model Parameter Estimation,* SIAM.

Tian, Y. & Ritzwoller, M.H., 2015. Directionality of ambient noise on the Juan de Fuca plate: implications for source locations of the primary and secondary microseisms, *Geophys. J. Int.,* **201**(1), 429–443.

Traer, J. & Gerstoft, P., 2014. A unified theory of microseisms and hum, *J. geophys. Res.,* **119**(4), 3317–3339.

Traer, J., Gerstoft, P., Bromirski, P.D. & Shearer, P.M., 2012. Microseisms and hum from ocean surface gravity waves, *J. geophys. Res.,* **117**(B11), B11307.

Tromp, J., Luo, Y., Hanasoge, S. & Peter, D., 2010. Noise cross-correlation sensitivity kernels, *Geophys. J. Int.,* **183,** 791–819.

Ward Neale, J., Harmon, N. & Srokosz, M., 2017. Improving microseismic P wave source location with multiple seismic arrays, *J. geophys. Res.,* **123**(1), 476–492.

Xu, Z., Mikesell, T.D. & Gribler, G., 2018, Source-distribution estimation from direct rayleigh waves in multicomponent crosscorrelations, in *SEG Technical Program Expanded Abstracts 2018,* pp. 3090–3094, Society of Exploration Geophysicists.

Xu, Z., Mikesell, T.D., Gribler, G. & Mordret, A., 2019. Rayleigh-wave multicomponent cross-correlation-based source strength distribution inversion. Part 1: theory and numerical examples, *Geophys. J. Int.,* **218**(3), 1761–1780.

Xu, Z., Mikesell, T.D., Umlauft, J. & Gribler, G., 2020. Rayleigh-wave multicomponent crosscorrelation-based source strength distribution inversions. Part 2: a workflow for field seismic data, *Geophys. J. Int.,* **222**(3), 2084–2101.

Yao, H. & van der Hilst, R.D., 2009. Analysis of ambient noise energy distribution and phase velocity bias in ambient noise tomography, with application to SE Tibet, *Geophys. J. Int.,* **179,** 1113–1132.

SUPPORTING INFORMATION

Supplementary data are available at *GJI* online.

Figure S1. Misfit development in all frequency bands. Crosses show the average misfit at each iteration in the respective frequency band (red: all, black: only measurements below the 90th percentile). The dashed green line indicates the estimated data uncertainty. All values are normalized by the original misfit (in iteration 0) for easier comparison.

Figure S2. Synthetic recovery test. Modified from Ermert *et al.* (2017).

Figure S3. Top row: model resulting after one iteration when a constraint is applied forcing hum sources to occur only in bodies of water (frequency band: 6–12 mHz). Bottom row: model after one iteration without the constraint. While there are few similarities, the updates are mostly different. The measurement used in the inversion tends to produce artifacts in the case of large areas without sources (see text for details).

Figure S4. Synthetic test, misfit evolution and comparison of target and recovered model. Top-left-hand panel: Comparison of PSD curves in selected locations, which are marked on the maps in the centre and right-hand column by green crosses and a distinct symbol designating each location. Bottom-left-hand panel: Misfit evolution. Central column: Normalized average amplification in two selected frequency bands for the target model. The dimensionless map coordinates are given as distance per shortest wavelength. Right-hand column: Same for inverted model. Black triangles denote receiver locations.

supplementary_anim.avi

Please note: Oxford University Press is not responsible for the content or functionality of any supporting materials supplied by the authors. Any queries (other than missing material) should be directed to the corresponding author for the paper.